

Thermal Based Damage Detection in Porous Materials

H. T. Banks^{1,*}, Brittany Boudreaux¹, Amanda Keck Criner¹, Krista Foster²,
Cerena Uttal³, Thomas Vogel⁴, William P. Winfree⁵

January 1, 2009

Abstract

We report here on the use of the heat equation to simulate a thermal interrogation method for detecting damage in a heterogeneous porous material. We first use probability schemes to randomly generate pores in a sample material; then we simulate flash heating of the compartment along one of its boundaries. Temperature data along the source and back boundaries are recorded and then analyzed to distinguish differences between the undamaged and damaged materials. These results suggest that it is possible to detect damage of a certain size within a porous medium using thermal interrogation.

Key Words: thermal interrogation, material with porosity, damage detection

¹Department of Mathematics and Center for Research in Scientific Computation, North Carolina State University, Raleigh, NC; ²Department of Mathematics, Youngstown State University, Youngstown, OH; ³Department of Mathematics, Mount Holyoke College, South Hadley, MA; ⁴Department of Mathematics, University of St. Andrews, St. Andrews, Fife, Scotland; ⁵Nondestructive Evaluation Sciences Branch, Mail Stop 231, NASA Langley Research Center, Hampton, VA.

E-mails: htbanks@ncsu.edu (*corresponding author), baboudre@ncsu.edu, akcriner@ncsu.edu, kmfoster01@student.yosu.edu, cerenauttal@yahoo.com, tv23@st-andrews.ac.uk, William.P.Winfree@nasa.gov.

1 Introduction

Nondestructive evaluation (NDE) is a very useful tool that enjoys widespread use in testing structures, especially as they age beyond their design life. Proper use of NDE can increase the safety and service life of components in aircraft, spacecraft, automobiles, trains, and piping. There are numerous viable NDE methods including ultrasound, magnetic particle imaging, eddy current, acoustic emission, and radiology to mention a few [17]. These methods have been successfully developed for a large range of problems, particularly for homogeneous metallic structures [3]-[7]. Composite materials are lighter and stronger than metallic materials, however, are inherently non-homogenous and often are fabricated with acceptable levels of porosity. These materials are used in many critical structures including aeronautical and aerospace vehicles, so there is a need to develop and evaluate NDE techniques for these materials [12, 19].

Active thermography is a particularly appropriate technique for materials with significant porosity. Active thermography measures the spatial and temporal evolution of the surface temperature following an input heat flux to detect subsurface anomalies. This evolution is a result of heat diffusion in the material. Since heat diffuses around porosity, rather than strongly interacting with it, thermography is able to detect large anomalies deep in a porous material. Additional advantages of thermal NDE are that it is a single sided, noncontacting and a large area technique making in-service evaluation feasible. It is also possible to embed temperature sensors in the material [18] for continuous structural health monitoring. We treat here the problem of thermal NDE in porous materials.

We describe a mathematical model for thermal transport in a two dimensional (2-D) porous material domain in Section 2. Using ideas based on the efforts in [8], we generated families of porous sample domains through various random geometry schemes. Methods for generation of these geometries are discussed in Section 3. We then discuss briefly the numerical solution of the model on such domains in Section 4. In Section 5 we report on subsequent use of the random geometry schemes with added damage due to oxidation of increasing sizes to the sample. For samples with and without damage due to oxidation, we carried out simulations to compare the resulting temperature profiles in space and time at both the source and back boundary. Graphical summaries of these simulations are also presented in Section 5. Finally, in Sections 6 and 7, we discuss the conclusions of our work and possible future directions of research, respectively.

2 Mathematical Model

We will model the 2-D problem for our proof of concept efforts here. Our 2-D geometries represent a small slice of a 3-D specimen as a rectangle with elliptical pores, as described in Section 3. We model thermal diffusion as the sample is heated along an edge for a short time with a laser or flash lamp on the front boundary, which we will refer to as the source boundary. We record the temperature on both the source boundary and the boundary opposite the source boundary (referred to as the back boundary) during and after the heating.

We examine a 2 mm by 1 mm rectangle $\hat{\Omega} = \{(x, y) | 0 \leq x \leq L_1, 0 \leq y \leq L_2\} = [0, 2] \times [0, 1]$ with randomly placed pores. Let Ω denote the rectangle minus N pores, which are given by

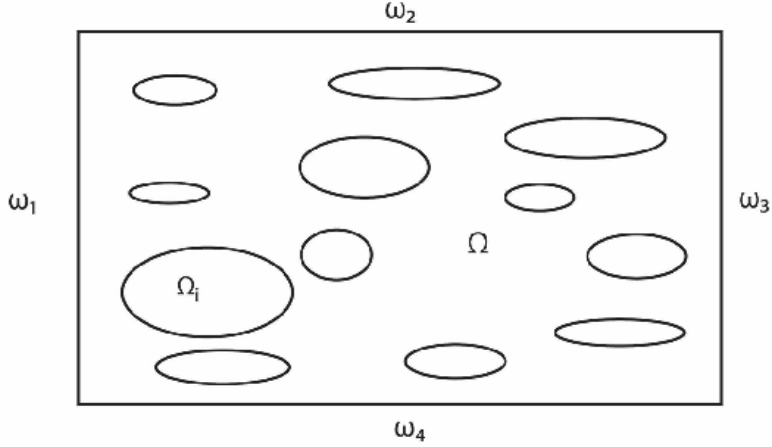


Figure 1: A typical example of a 2-D specimen

$\Omega_1, \Omega_2, \dots, \Omega_N$. The domain of interest is then $\hat{\Omega} = \Omega \cup (\cup_{i=1}^N \Omega_i)$. The exterior boundary of Ω has 4 edges, which we denote by ω_j where $j=1, \dots, 4$; thus $\partial\hat{\Omega} = \cup_{j=1}^4 \omega_j$. It is assumed that each pore Ω_i has a smooth boundary with Ω given by $\partial\Omega_i$, as depicted in Figure 1.

The 2-D heat diffusion equation, which describes heat as it diffuses through a region, is based on Fourier's law and is given [10, 13] by

$$\rho(x, y)c_p(x, y)\frac{\partial u(t, x, y)}{\partial t} = \nabla \cdot (k(x, y)\nabla u(t, x, y)). \quad (1)$$

Here $u(t, x, y)$ is the temperature, $\rho(x, y)$ is the material density of the sample, $c_p(x, y)$ is the specific heat of the material, and $k(x, y)$ is the thermal conductivity. We observe that the coefficients are functions in space which have jump discontinuities at $\partial\Omega_i$ for $i = 1, 2, \dots, N$. Thus $k(x, y)$ is not differentiable and therefore in general solutions $u(t, x, y)$ are not twice differentiable in space. Hence the above formulation is clearly inadequate for our problems. We use a variational or weak formulation to avoid these concerns [7].

Let k_p denote the thermal conductivity of the pores and k_m denote that of the material. Thus, the rectangular sample has thermal conductivity

$$k(x, y) = \begin{cases} k_p, & (x, y) \in \Omega_i, i = 1, \dots, N, \\ k_m, & (x, y) \in \Omega. \end{cases} \quad (2)$$

Consider test functions $\phi \in H^1(\hat{\Omega})$, in an integrated form of (1) given by

$$\int_{\hat{\Omega}} c_p(x, y)\rho(x, y)\frac{\partial u}{\partial t}\phi(x, y)dA = \int_{\hat{\Omega}} \phi(x, y)\nabla \cdot (k(x, y)\nabla u)dA. \quad (3)$$

We rewrite this integral form by decomposing the domain $\hat{\Omega}$ into Ω and $\Omega_1, \Omega_2, \dots, \Omega_N$. Note that

k is constant in each subregion. We find

$$\begin{aligned} & \int_{\hat{\Omega}} c_p(x, y) \rho(x, y) \frac{\partial u}{\partial t} \phi(x, y) dA \\ &= k_m \int_{\Omega} \phi(x, y) \nabla \cdot (\nabla u) dA + k_p \sum_{i=1}^N \int_{\Omega_i} \phi(x, y) \nabla \cdot (\nabla u) dA. \end{aligned} \quad (4)$$

We use Green's first identity to obtain

$$\begin{aligned} & \int_{\hat{\Omega}} c_p(x, y) \rho(x, y) \frac{\partial u}{\partial t} \phi(x, y) dA \\ &= \sum_{j=1}^4 \left(k_m \int_{\omega_j} \phi(x, y) (\nabla u \cdot \hat{n}_j) ds \right) - k_m \int_{\Omega} \nabla u \cdot \nabla (\phi(x, y)) dA \\ &+ k_p \sum_{i=1}^N \left(\int_{\partial\Omega_i} \phi(x, y) (\nabla u \cdot \hat{n}_i) ds - \int_{\Omega_i} \nabla u \cdot \nabla (\phi(x, y)) dA \right). \end{aligned} \quad (5)$$

The terms $\sum_{i=1}^N k_p \int_{\partial\Omega_i} \phi(x, y) (\nabla u \cdot \hat{n}_i) ds$ pose a problem because this integration requires knowledge of the locations of the pores; this is in general unknown. However, if one assumes negligible heat flux on the boundaries between material and air (a physically reasonable assumption for most applications), then $\nabla u \approx 0$ on $\partial\Omega_i$ and hence $\sum_i k_p \int_{\partial\Omega_i} \phi(x, y) (\nabla u \cdot \hat{n}_i) ds = 0$.

Combining the three remaining terms from (5), we find

$$\begin{aligned} & \int_{\hat{\Omega}} c_p(x, y) \rho(x, y) \frac{\partial u}{\partial t} \phi(x, y) dA \\ &= \sum_{j=1}^4 \left(k_m \int_{\omega_j} \phi(x, y) (\nabla u \cdot \hat{n}_j) ds \right) - \int_{\hat{\Omega}} k(x, y) \nabla u \cdot \nabla \phi(x, y) dA. \end{aligned} \quad (6)$$

Excluding the source boundary, we assume an insulated rectangle so that $\nabla u = 0$ on the boundaries ω_1, ω_2 , and ω_3 . The ω_4 or source boundary, which consists of the region $\{(x, 0) | 0 \leq x \leq L_1\}$, acts as a source for an initial period and is subsequently insulated. We represent the corresponding boundary condition with the characteristic function

$$k_m \nabla u \Big|_{\omega_4} = S_0 \chi_{[t_0, t_s]}(t) = \begin{cases} S_0, & t \in [t_0, t_s] \\ 0, & \text{otherwise.} \end{cases} \quad (7)$$

Thus we have

$$\int_{\hat{\Omega}} c_p \rho \frac{\partial u}{\partial t} \phi dA = \int_0^{L_1} \phi(x, 0) S_0 \chi_{[t_0, t_s]}(t) dx - \int_{\hat{\Omega}} k \nabla u \cdot \nabla \phi dA. \quad (8)$$

This weak formulation is employed in the MATLAB Partial Differential Equation Toolbox 1 (PDE toolbox) to provide numerical solutions to the system; this will be discussed further in Section 4.

3 Generation of Random Geometries

A major component of the effort reported on here involves generation of domains with randomly placed pores of different sizes as depicted in Figure 1 and Figures 3-12. We concentrated our efforts on elliptical shaped pores with semi-major axes in the horizontal (x) direction. This was motivated by visual inspection of material samples at NASA as depicted in Figure 2.

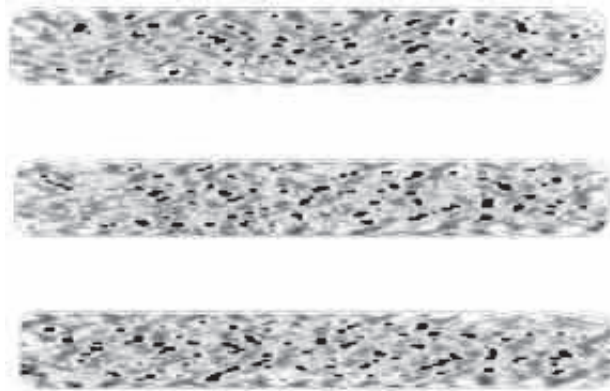


Figure 2: An example of a porous specimen.

We model porosity by randomly placing pores in an $L_1 = 2$ mm by $L_2 = 1$ mm rectangle $\hat{\Omega} = [0, 2] \times [0, 1]$ employing ideas developed in [8]. The pores are ellipses to represent voids in a two-dimensional slice of any piece of porous material. For simplicity in algorithm development, we began carrying out our simulations with circles (see [9] for discussions) but subsequently used ellipses for more realistic representations. Even though pores coalesce when they intersect physically, we assume that the pores do not overlap with each other or the boundaries of the rectangular compartment (more irregular shapes in pores could be achieved by allowing overlaps). To do this, in our algorithms we first generate a pore using one of the probability schemes described below. The pore is then placed in the compartment if it does not overlap with an existing pore, and rejected if it does. Another pore is then randomly selected as described below, etc., until the desired porosity of the material is achieved.

3.1 Ellipses: Uniformly Distributed Centers, Bi-Normally Distributed Semi-Axes

We used several probability schemes to generate random ellipses in the compartment $\hat{\Omega}$. The percent porosity, or percent surface area covered by the pores, is an input for each algorithm. We considered pores described by ellipses centered at (\tilde{x}, \tilde{y}) having semi-major axis a and semi-minor axis b and hence represented by

$$\left(\frac{x - \tilde{x}}{a}\right)^2 + \left(\frac{y - \tilde{y}}{b}\right)^2 = 1 \quad (9)$$

. The algorithm that we illustrate here created ellipses using a uniform distribution for both the \tilde{x} and \tilde{y} coordinates of the centers and a bi-normal distribution for the semi-major and semi-minor axes a, b . In this algorithm, we also permitted two sizes of ellipses using a discrete binomial distribution selecting between smaller ellipses (with a probability of .89) and larger ellipses (with a probability of .11).

3.2 Oxidation

To simulate pore-like damages due to oxidation, we first generate one unusually large ellipse (see Section 5 for examples) to represent damage and then placed pores using the distributions described above. When generating various elliptical damages, the center was an input. The semi-major axis for damage was taken as an input, and the semi-minor axis was calculated so as to maintain a constant ratio between the two axes as we chose damages of different sizes.

4 Numerical Solutions

After generating a particular geometry, we solved the heat equation (8) using PDE Toolbox with the parameters summarized in Table 1.

Heat transfer coefficient	S_0	$3.3 \times 10^4 \frac{\text{erg}}{\text{mm}^2}$
Material thermal conductivity	k_m	$35000 \frac{\text{erg}}{\text{mm}^\circ\text{K sec}}$
Heat capacity	c_p	$7.5 \times 10^6 \frac{\text{erg}}{\text{g}^\circ\text{K}}$
Density	ρ	$1.6 \times 10^{-3} \frac{\text{g}}{\text{mm}^3}$

Table 1: Parameter values

As already noted, three of the compartment's four sides are insulated and defined by Neumann boundary conditions where heat flux is zero. The source boundary has a heat transfer coefficient of $3.3 \times 10^4 \text{ erg/mm}^2$ during flash heating and zero flux later. There is also zero heat flux on the boundaries between the material and the pores; we took pore conductivity $k_p = 0$. PDE Toolbox creates a mesh using the Delaunay triangulation algorithm and reduces the parabolic equation into elliptic equations which are solved with the Finite Element Method; see [14] for details. The reduction to elliptic equations assumes time-independence of the boundary conditions; however, recall we have a time-dependent source boundary. We avoid the associated computational difficulties by solving the PDE on the interval $[t_0, t_s]$ and then on $t \geq t_s$, observing that the boundary conditions are time-independent on these intervals. The final time for the first solution is t_s , which is the initial time for the second solution and $u(t_s, x, y)$ is used as the initial condition for the second solution to guarantee continuity in time. These two solutions are combined to provide a solution over the entire time interval of interest.

We validated the convergence of PDE Toolbox’s numerical solution as outlined in [9] to achieve precision adequate for our investigations (e.g., 0.04 °K for 2% porosity samples and approximately 0.1 °K for samples with 5% and 10% porosity).

5 Results

We generated numerous samples with varying levels of porosity including 2%, 5% and 10% and with a single damage of varying size located near the source surface, the back surface or mid sample. A large number of results for simulations with these geometries are given in [9]. We summarize in Table 2 below the means \bar{a}_i and \bar{b}_i along with their standard deviations σ_{a_i} and σ_{b_i} for the semi-major and semi-minor axes of the pores over all the geometries.

Semi-axes for samples with 2% porosity	
Means	Standard deviations
$\bar{a}_1 = 1.856 \times 10^{-2}$	$\sigma_{a_1} = 1.547 \times 10^{-3}$
$\bar{b}_1 = 6.188 \times 10^{-3}$	$\sigma_{b_1} = 5.156 \times 10^{-4}$
$\bar{a}_2 = 3.156 \times 10^{-2}$	$\sigma_{a_2} = 2.250 \times 10^{-3}$
$\bar{b}_2 = 1.051 \times 10^{-2}$	$\sigma_{b_2} = 7.514 \times 10^{-4}$

Semi-axes for samples with 5% porosity	
Means	Standard deviations
$\bar{a}_1 = 2.935 \times 10^{-2}$	$\sigma_{a_1} = 2.446 \times 10^{-3}$
$\bar{b}_1 = 9.784 \times 10^{-3}$	$\sigma_{b_1} = 8.154 \times 10^{-4}$
$\bar{a}_2 = 4.990 \times 10^{-2}$	$\sigma_{a_2} = 3.564 \times 10^{-2}$
$\bar{b}_2 = 1.663 \times 10^{-2}$	$\sigma_{b_2} = 1.188 \times 10^{-3}$

Semi-axes for samples with 10% porosity	
Means	Standard deviations
$\bar{a}_1 = 4.151 \times 10^{-2}$	$\sigma_{a_1} = 3.459 \times 10^{-3}$
$\bar{b}_1 = 1.384 \times 10^{-2}$	$\sigma_{b_1} = 1.153 \times 10^{-3}$
$\bar{a}_2 = 7.057 \times 10^{-2}$	$\sigma_{a_2} = 5.041 \times 10^{-3}$
$\bar{b}_2 = 2.352 \times 10^{-2}$	$\sigma_{b_2} = 1.680 \times 10^{-3}$

Table 2: Means and standard deviations for a_1 and b_1 , the semi-major and semi-minor axes of the smaller pores, and a_2 and b_2 , the semi-axes of the larger pores.

We present here a sampling of representative graphical results from [9]. Each group of figures below depicts a compartment both with and without damage and the corresponding temperature profiles. Observe that the pores surrounding the damage are identical to those in the undamaged

compartment. In every case, we heat the source boundary for 0.6 seconds and record the temperature a total of 1.3 seconds (including heating time). Figures 3-7 and Figures 11-12 present results for samples of varying percent porosity with damages of various size located near the source surface. Figure 8 depicts results for mid sample damage while Figures 9 and 10 give results for samples with damage near the back boundary.

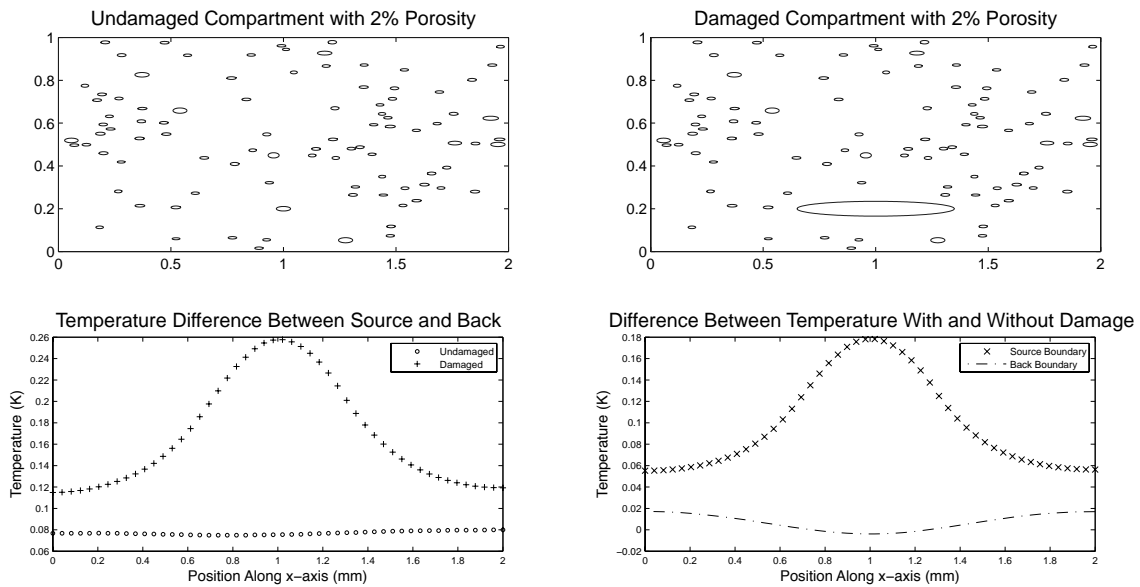


Figure 3: Sample with 2% porosity, damage centered at (1, 0.2), semi-major axis $a = 0.35$ mm, semi-minor axis $b = 0.0346$ mm.

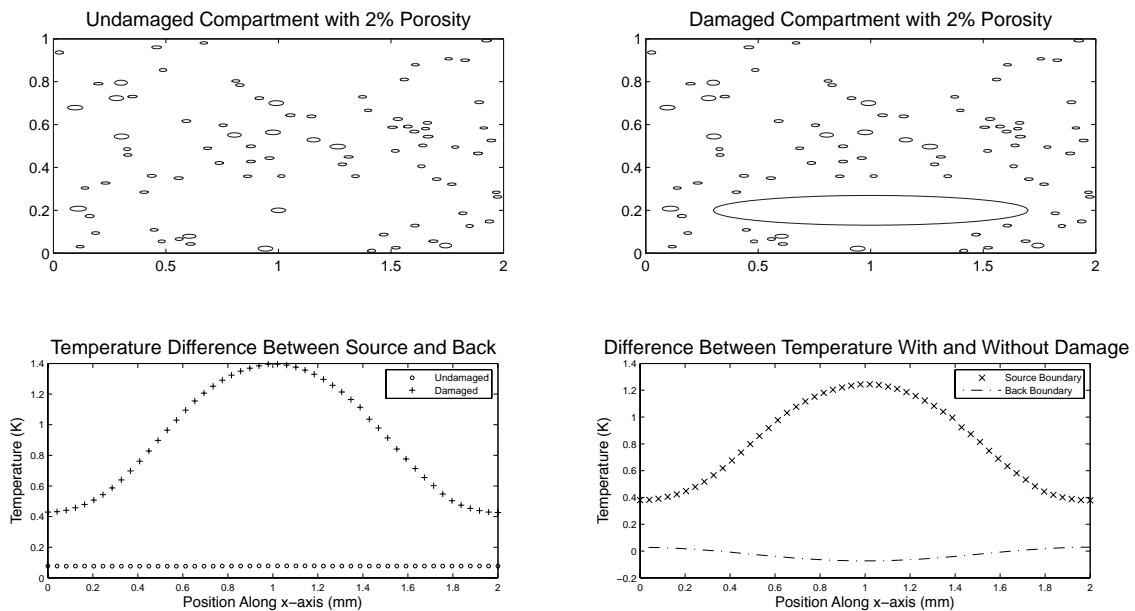


Figure 4: Sample with 2% porosity, damage centered at (1, 0.2), semi-major axis $a = 0.7$ mm, semi-minor axis $b = 0.0692$ mm.

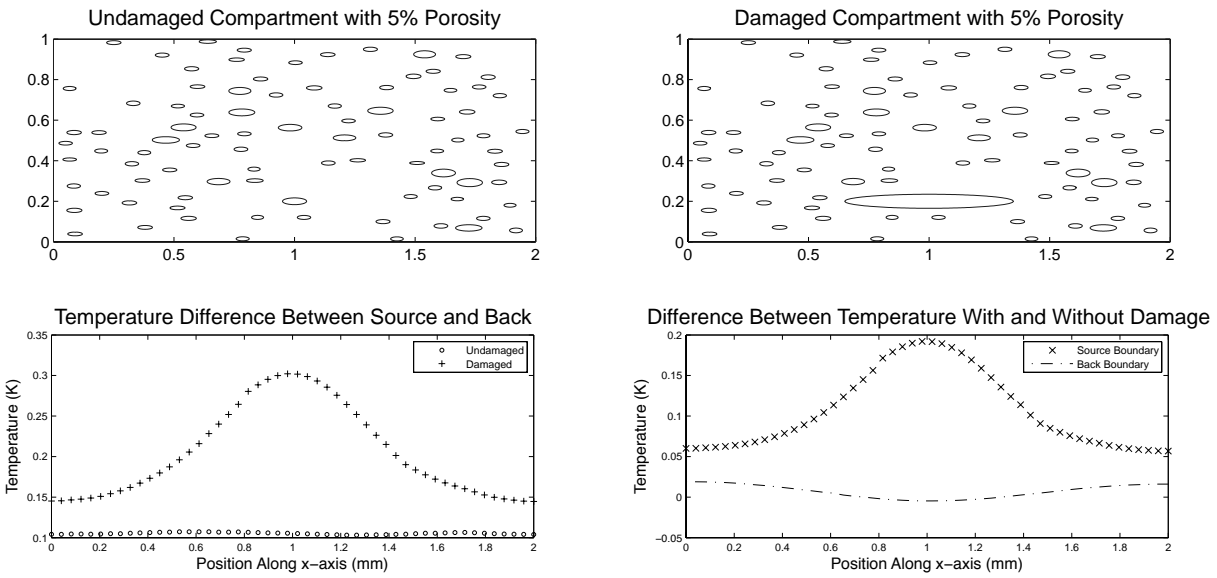


Figure 5: Sample with 5% porosity, damage centered at (1, 0.2), semi-major axis $a = 0.35$ mm, semi-minor axis $b = 0.0346$ mm.

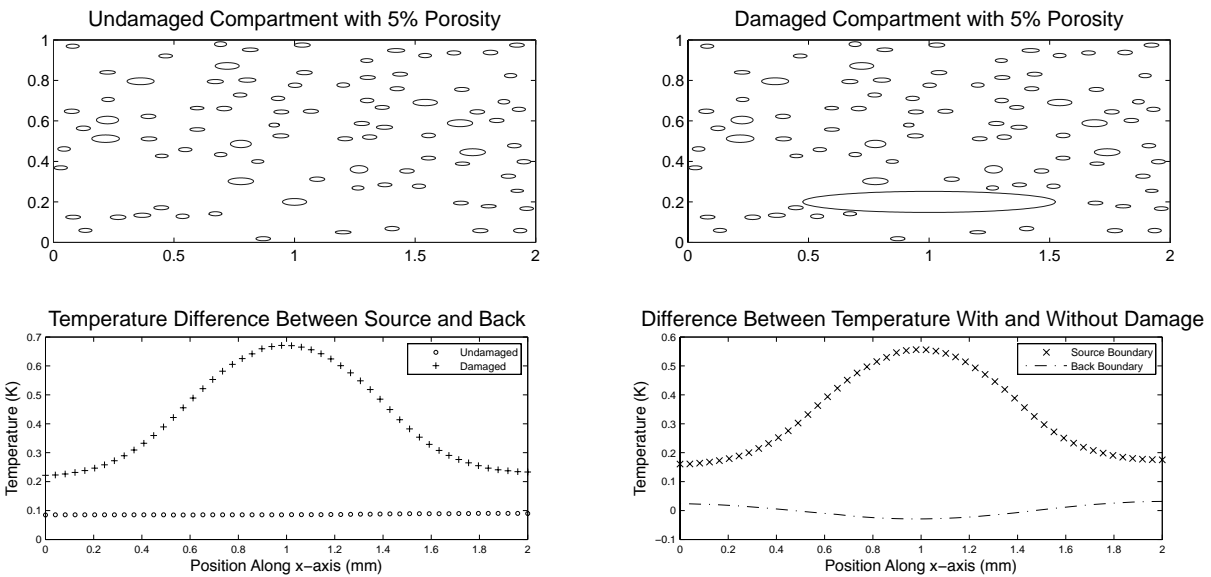


Figure 6: Sample with 5% porosity, damage centered at (1, 0.2), semi-major axis $a = 0.525$ mm, semi-minor axis $b = 0.0519$ mm.

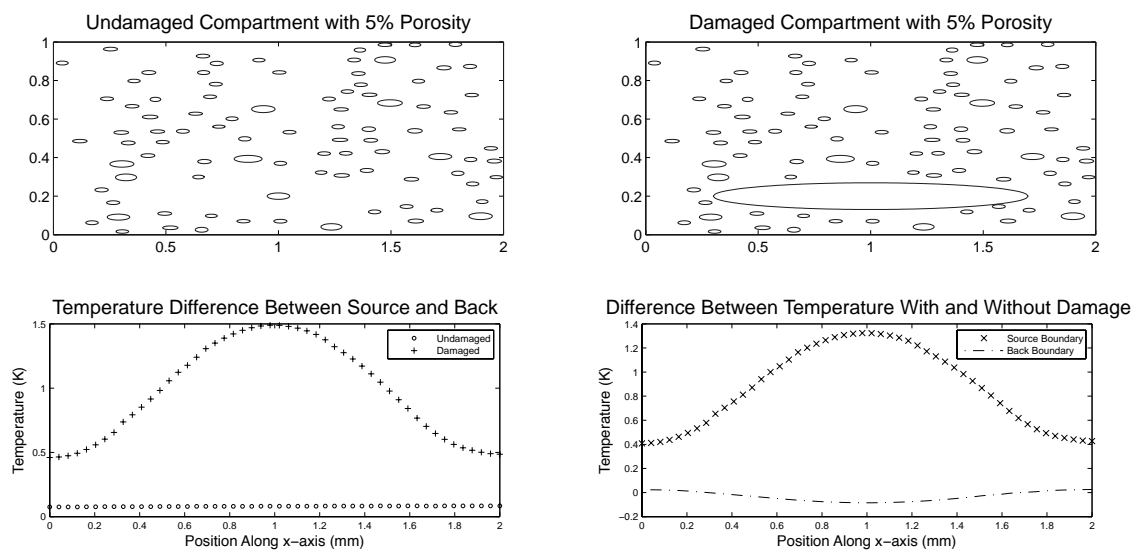


Figure 7: Sample with 5% porosity, damage centered at (1, 0.2), semi-major axis $a = 0.7$ mm, semi-minor axis $b = 0.0692$ mm.

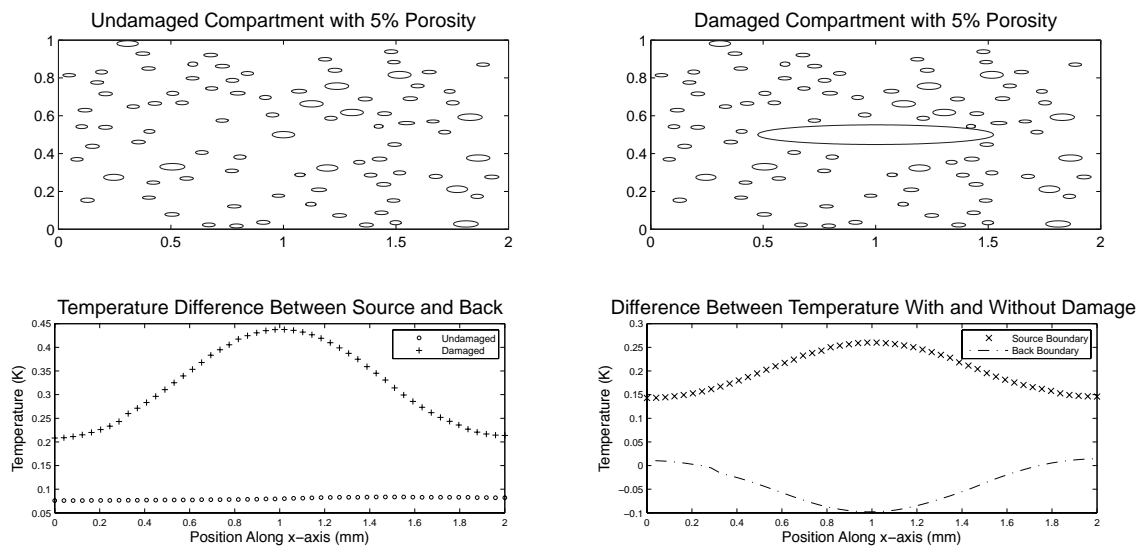


Figure 8: Sample with 5% porosity, damage centered at (1, 0.5), semi-major axis $a = 0.525$ mm, semi-minor axis $b = 0.0519$ mm.

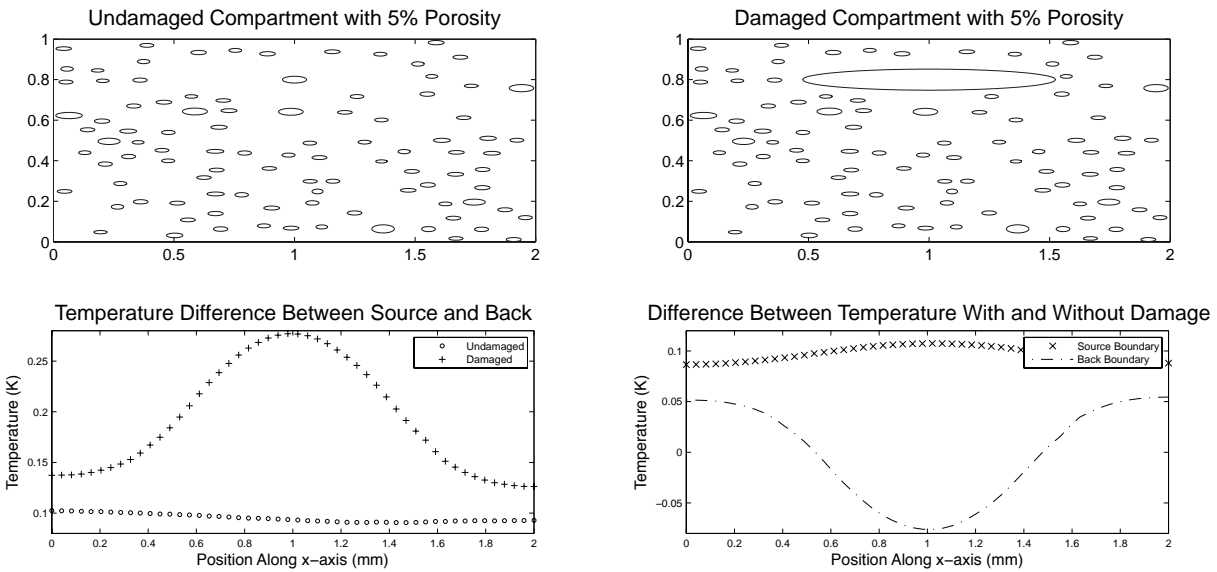


Figure 9: Sample with 5% porosity, damage centered at (1, 0.8), semi-major axis $a = 0.525$ mm, semi-minor axis $b = 0.0519$ mm.

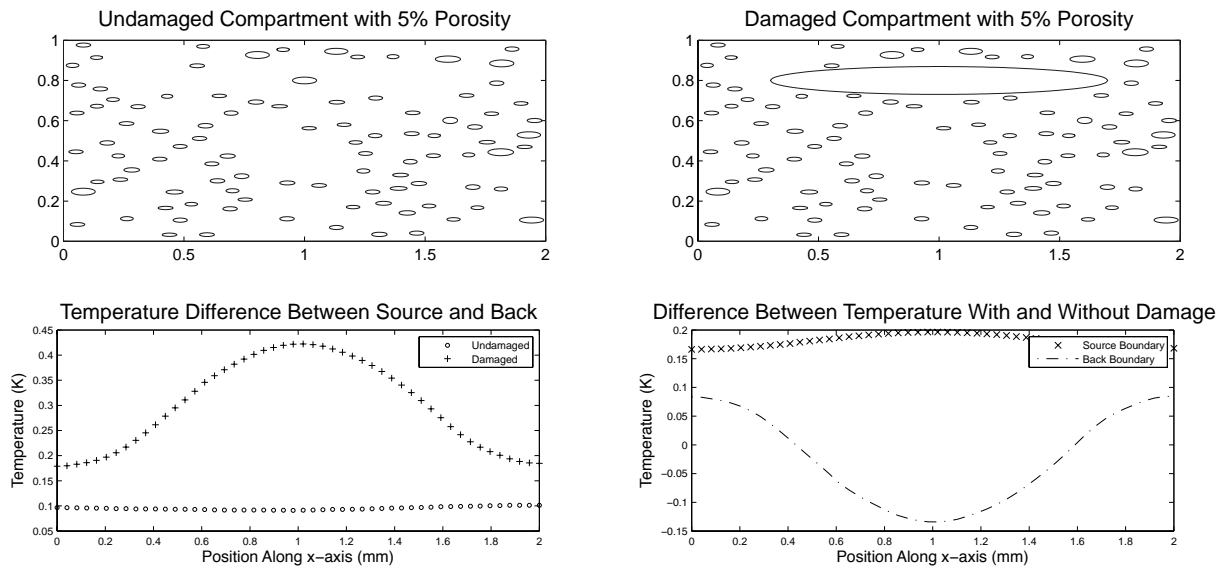


Figure 10: Sample with 5% porosity, damage centered at (1, 0.8), semi-major axis $a = 0.7$ mm, semi-minor axis $b = 0.0692$ mm.

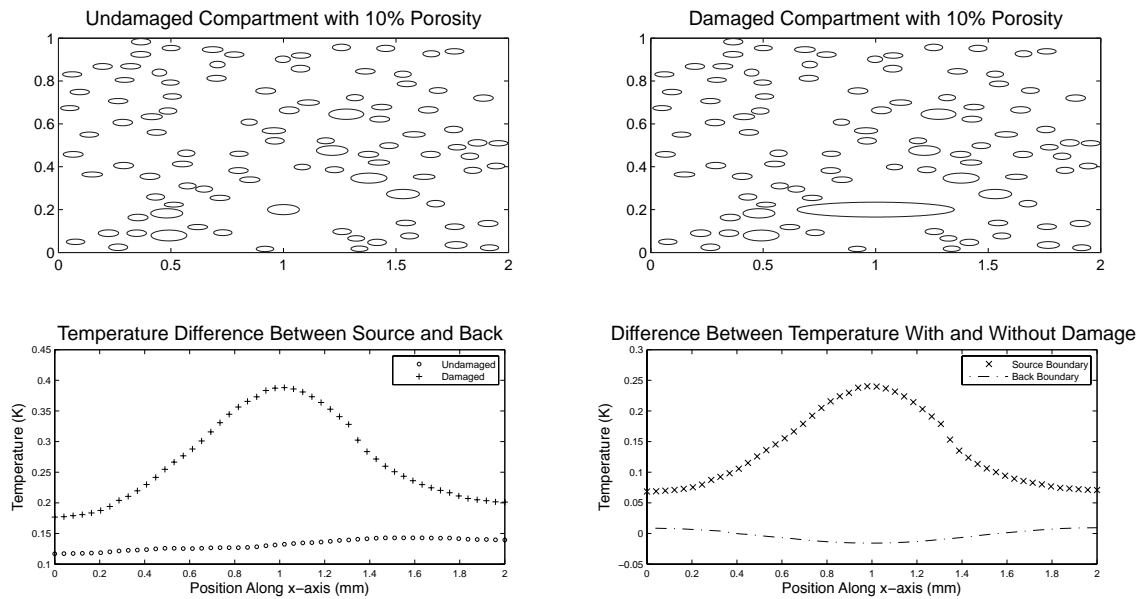


Figure 11: Sample with 10% porosity, damage centered at (1, 0.2), semi-major axis $a = 0.35$ mm, semi-minor axis $b = 0.0346$ mm.

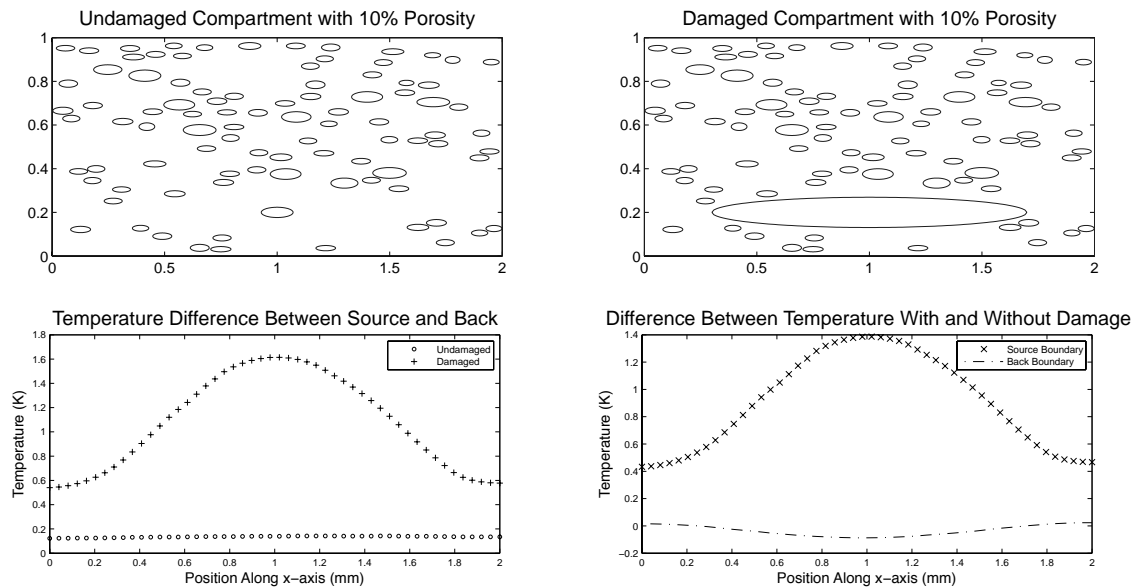


Figure 12: Sample with 10% porosity, damage centered at (1, 0.2), semi-major axis $a = 0.7$ mm, semi-minor axis $b = 0.0692$ mm.

6 Discussion and Conclusions

We observed several general trends in our temperature profile graphs. First, we tracked temperatures at the source and back boundaries so as to shed light on possible sensor placement if options were available. As might be expected, we found that the absolute value of the difference between damaged and undamaged material is greatest at the center of the damage due to oxidation. At 2% porosity with a damage due to oxidation width of 0.7 mm near the source boundary, the maximum difference between the damaged and undamaged material is approximately 0.18 °K at the source boundary and 0.02 °K at the back boundary; this is depicted in Figure 3. As shown in Figure 4, at a damage width of 1.4 mm due to oxidation, the maximum difference is 1.2 °K at the source boundary and 0.03 °K at the back boundary. In Figure 5, we see that at 5% porosity, the maximum difference between undamaged and damaged material at the source boundary is 0.2 °K while at the back boundary the maximum difference is 0.02 °K for a damage width of 0.7 mm. In Figure 7, when the damage width increases to 1.4 mm, the maximum difference is 1.35 °K at the source boundary and 0.08 °K at the back boundary. At 10% porosity, the maximum difference is 0.24 °K at the source boundary and 0.02 °K at the back boundary for a damage width of 0.7 mm, as seen in Figure 11. When the size of the damage is increased to a width of 1.4 mm, we find in Figure 12 that maximum temperature difference is 1.4 °K at the source boundary and 0.09 °K at the back boundary. These observations demonstrate that the maximum temperature difference between damaged and undamaged material at the source boundary is larger than at the back boundary when the damage is placed near the source boundary. We anticipate that with a sensor that has 0.1 °K resolution, placed on the source boundary, we will be able to detect 0.7 and 1.4 mm damages due to oxidation in materials with 2, 5, or 10% porosity. With the same sensor placed on the back boundary, we would not expect to be able to detect these damages in any of the materials.

The difference between damaged and undamaged material is greatest at the center of the damage due to oxidation for both the source and back boundary measurements in most of our computations. The source boundary temperature is always higher with damage, whereas the back boundary temperature is lower with damage in most of our computations. When the damage is placed near the source boundary, the absolute value of the temperature difference resulting from the damage is much greater for the source boundary than the back boundary. When the damage is placed at the center of the compartment, the absolute value of the temperature difference is approximately the same for the source and back boundaries. And lastly, when the damage is placed near the back boundary, the absolute value of the the temperature difference is much greater for the back boundary than the source boundary. At 5% porosity, for example, a 1.05 mm wide damage placed near the source boundary results in a 0.57 °K change in temperature at the source boundary and a 0.02 °K change in temperature at the back boundary; this is depicted in Figure 6. When the same sized damage is placed in the middle of the compartment, one can see a 0.25 °K change in temperature at the source boundary and a 0.11 °K change in temperature at the back boundary, as shown in Figure 8. When the damage is placed near the back boundary, one can see a 0.1 °K change in temperature at the source boundary and a 0.08 °K change in temperature at the back boundary (note that the magnitude of the temperature change decreases as the damage moves away from the source boundary); see Figure 9. These observations are important because they help to better iden-

tify the location of the damage. In Figure 5, for example, at 5% porosity, a damage of width 0.7 mm centered near the source boundary results in a temperature difference of 0.19 °K at the source boundary. Meanwhile, in Figure 10, at the same porosity, a damage of width 1.4 mm near the back boundary gives an equal temperature difference. When we consider the change in temperature (the maximum difference minus the minimum difference), however, we are able to determine the location of the damage. When the damage is centered near the back, the change in temperature is 0.22 °K for the back boundary and only 0.03 °K for the source boundary. As depicted in Figure 7, when the damage is centered near the source, the change in temperature at the source is 0.89 °K, and 0.11 °K for the back boundary. Thus, by comparing sensors at the back surface with those at the source surface, one should be able to discern the depth of the damage if it is of sufficient size.

We also observed two general trends in the temperature vs. time graphs (in results given in [9] but not depicted here). As the size of the damage due to oxidation grows, it takes longer for the system to reach thermal equilibrium. The farther away the damage is from the source boundary, the closer together the source and back boundary temperatures are for both $x = 1$ and $x = 0$.

7 Further Work

The results developed here not only provide useful information regarding the detection of damage due to oxidation, but also provide methods of generating synthetic data that may be used for further analysis as well. We would like to develop a method of separating the effect of porosity (which might reasonably be viewed as random noise) from the effect of damage in effective thermal diffusivity. In order to do this, we must develop parameter estimation techniques. There are various methods which use flash heating to estimate the effective thermal diffusivity; some of these methods are discussed in [10] and [15]. We also plan on investigating homogenization and the limits of its usefulness in detecting damages in porous materials. Homogenization theory assumes periodicity in the coefficients of the partial differential equation. The usual theory [11] requires that periodicity go to zero in some sense. The periodicity of the coefficients is a result of periodic geometry (for instance we could have a geometry with an infinite number of infinitely small circles within a rectangle) though homogenization can be applied to more complex geometries [1, 2]. If there are not many pores or the pores are too large, we expect homogenization will not provide a good approximation, while if we have a high number of small pores, we suspect homogenization will be a good approximation. There are many advantages to using homogenization theory. After a limit is taken, we are left with a constant coefficient partial differential equation on a homogeneous square, which is readily treated numerically. Also, homogenization can be used in n dimensions. Damage here is neither “small” nor “periodic”, so homogenization cannot be used to study this aspect of our problem. We hope to use homogenization theory both in a local or regional sense (i.e., near surface vs. deep interrogations) to determine the effects of the porosity in the early time behavior of the thermal diffusivity and then remove this effect from later time behavior to gain a resolved effect of the damage as reflected in the thermal diffusivity or conductivity [16]. Of course, to be useful as a basis for a widely applicable interrogation technology, these investigations must eventually be carried out for three dimensional geometries with random porosities.

8 Acknowledgments

This research, which was begun as part of an REU project at North Carolina State University for co-authors BB, KF, CU, and TV, which was supported in part by the National Science Foundation (NSF) under grant DMS-0552571, and in part by the National Security Agency under grant H98230-08-1-0094. It was also supported in part (AKC) by the National Science Foundation (NSF) under grant DMS-0636590, and in part (HTB and AKC) by NASA under grant NIA/NCSU-03-01-2536-NC.

References

- [1] E. Acerbi, V. C. Piat, G. D. Maso, and D. Percivale, An extension theorem from connected sets, and homogenization in general periodic domains, *Nonlinear Analysis: Theory, methods and applications*, **18** (1992), 481–496.
- [2] N. S. Bakhvalov and J. S. J. Paulin, Homogenization for thermoconductivity in a porous medium with periods of different orders in the different directions, *Asymptotic Analysis*, **13** (1996), 253–276.
- [3] H. T. Banks, N. L. Gibson, and W. P. Winfree, Void detection in complex geometries, Center for Research in Scientific Computation Technical Report, CRSC-TR08-09, NCSU, May, 2008.
- [4] H. T. Banks, M. L. Joyner, B. Wincheski, and W. P. Winfree, Nondestructive evaluation using a reduced-order computational methodology, *Inverse Problems*, **16** (2000), 929–945.
- [5] H.T. Banks and F. Kojima, Boundary shape identification problems in two-dimensional domains related to thermal testing of materials, *Quarterly of Applied Mathematics*, **47** (1989), 273–293.
- [6] H. T. Banks and F. Kojima, Identification of material damage in two-dimensional domains using the SQID-based nondestructive evaluation system, *Inverse Problems*, **18** (2002), 1831–1855.
- [7] H. T. Banks, F. Kojima, and W. P. Winfree, Boundary estimation problems arising in thermal tomography, *Inverse Problems*, **6** (1990), 897–921.
- [8] K. L. Bihari, *Analysis of Thermal Conductivity in Composite Adhesives*, PhD thesis, North Carolina State University, Raleigh, 2001.
- [9] B. Boudreaux, K. Foster, C. Uttal, T. Vogel, H.T. Banks, A.K. Criner, and W.P. Winfree, *Thermal Interrogation of Porous Materials*, Center for Research in Scientific Computation Technical Report CRSC-TR08-11, North Carolina State University, Raleigh, September, 2008.

- [10] H. S. Carslaw and J. C. Jaeger, *Conduction of Heat in Solids*, Oxford University Press, 1959.
- [11] D. Cioranescu and P. Donato, *An Introduction to Homogenization*, Oxford University Press, 1999.
- [12] K. E. Cramer, W. P. Winfree, K. Hodges, A. Koshti, D. Ryan, and W. W. Reinhardt, Status of thermal NDT of space shuttle materials at NASA, in *9th Joint FAA/DoD/NASA Conference on Aging Aircraft*, 2007.
- [13] F. Incropera and D. Dewitt, *Fundamentals of Heat and Mass Transfer*, John Wiley & Sons, New York, 1990.
- [14] The Mathworks, Inc., *Partial Differential Equation Toolbox 1: User's Guide*, 2008.
- [15] W. J. Parker, R. J. Jenkins, C. P. Butler, and G. L. Abbott, Flash method of determining thermal diffusivity, heat capacity, and thermal conductivity, *Journal of Applied Physics*, **32** (1961), 1679–1684.
- [16] S Schmauder and U. Weber, Modelling of functionally graded materials by numerical homogenization, *Archive of Applied Mechanics*, **71** (2001), 182–192.
- [17] P. J. Shull (ed.), *Nondestructive Evaluation: Theory, Techniques, and Applications*, Marcel Dekker, Inc., 2001.
- [18] A. Stewart, G. Carman, and L. Richards, Nondestructive evaluation technique utilizing embedded thermal fiber optic sensors, *Journal of Composite Materials*, **37** (2003), 2197–2206.
- [19] W. P. Winfree, E. I. Madaras, K. E. Cramer, P. A. Howell, K. L. Hodges, J. P. Seebo, and J. L. Grainger, NASA Langley inspection of rudder and composite tail of American Airlines flight 587, in *46th AIAA/ASME/ASCE/AHS/ASC Structures, Structural Dynamics and Materials Conference*, 2005.